Journal of Materials Chemistry C

Exploring Thermal Transitions in Anthradithiophene-based Organic Semiconductors to Reveal Structure-Packing Relationships

Journal:	*Journal of Materials Chemistry C*
Manuscript ID	TC-ART-08-2018-003976.R1
Article Type:	Paper
Date Submitted by the Author:	12-Sep-2018
Complete List of Authors:	Li, Shi; University of Kentucky, Chemistry Ryno, Sean ; University of Kentucky, Chemistry Risko, Chad; University of Kentucky, Chemistry

Exploring Thermal Transitions in Anthradithiophene-based Organic Semiconductors to Reveal Structure-Packing Relationships

Shi Li, Sean M. Ryno, & Chad Risko

Department of Chemistry &
Center for Applied Energy Research
University of Kentucky
Lexington, Kentucky 40506 USA

Corresponding author: chad.risko@uky.edu

Abstract

Thermal analyses provide macroscopic measures as to how molecular-scale features impact the solid-state packing of organic semiconductors. Here, we make use of molecular dynamics simulations to explore the phase transitions of a series of anthradithiophene-based molecular materials. Various models are explored to overcome superheating effects that are typically associated with the simulated annealing of crystalline materials using periodic boundary conditions. Slab models, in particular, are shown to provide good agreement with melt temperatures determined experimentally, especially for unsubstituted anthradithiophenes. Importantly, the simulations provide atomic-scale details regarding solid-solid and solid-liquid phase transitions that deliver key insights into how variations in the anthradithiophene chemistry impact the nature of the molecular packing and, in turn, can be used to enhance the rational engineering of crystal packing in these organic semiconductors.

Introduction

Organic semiconductors (OSC), materials derived from π-conjugated organic molecules and polymers, offer distinctive form factors that are difficult for traditional inorganic semiconductors to match. Coupled with the capabilities of organic synthetic chemists to design and adapt molecule and polymer structure to direct moleuclar and material properties, OSC can enable the development of new generations of electronic and power generation and storage devices across a spectrum of applications, including thin-film transistors (OTFT), light-emitting diode (OLED) displays and lighting, electronic skins, electronic textiles, bioelectronics, sensors, photovoltaic (OPV) cells, and thermoelectrics, to name a few examples. OSC performance in any device architecture is dictated by a hierarchal morphology, starting with intermolecular interactions (i.e. exchange repulsion, dispersion, electrostatics, and induction)[1-9] that define local molecular packing and electronic interactions through long range (dis)order that can, for instance, dictate the mobility of charge carriers through the material, mechanical characteristics, and operational stability.[2, 5, 6, 10-19] Currently, the OSC community relies mostly on trial-and-error approaches to design, create, and apply OSC, as there are few rational guidelines that can direct the chemistry and processing to control material assembly or organization. To move away from such Edisonian approaches, direct correlations among these parameters need to be made, necessitating the advance of synthetic, analytical, and computational/theoretical techniques and the development and application of models that can probe this complex morphological hierarchy.

Thermoanalytical techniques – which can provide details of phase transitions, such as the glass transition (T_g), melt transition (T_m), and crystallization temperatures (T_c) – are particularly useful experimental tools to gauge the strengths of and interplay between intermolecular interactions and packing arrangements in OSC.[20-23] Data from such techniques, however, are inherently macroscale

and provide a time and space averaged result for a given sample, limiting the amount of microscopic insight can be obtained and provided as feedback for synthetic chemists interested in controlling solid-state packing and materials characteristics through molecular design. Hence, computational approaches that can probe these types of thermal transitions with atomic-scale resolution can provide invaluable connections with experiment.[24-26]

Classical molecular dynamics (MD) approaches, which bridge the gap between size-limited quantum mechanical calculations and macroscopic experimental analyses, are widely employed to explore phase transitions, as they are capable of simulating thousands to millions of atoms on time-scales that approach relevance to capture such events.[23, 27-29] A critical issue that needs to be overcome when implementing MD simulations to study thermal transitions is the so-called superheating effect,[28, 30-32] which can lead to overestimates of $1.2\times T_m$.[30, 33] Superheating has been attributed to (i) the periodic boundary conditions (PBC) used during the MD simulations (*i.e.* an infinite, periodic system is being heated equally throughout its entirety) and (ii) the large-temperature ranges that are traversed over very short timescales (in particular with respect to experiment) during the simulations. PBC can also be problematic as they may not account for the interfaces, defects, or disorder that one might expect for a real material, *i.e.*, sites in the material where one might expect phase transformations to first begin. To overcome this limitation, Jayaraman and co-workers[34] suggested the introduction of voids into simulated atomic crystals, wherein random point/atom deletions are made within a crystal to create disorder. Alternatively, Takahashi and co-workers simulated polymer melting using explicit surfaces and found that the melting at the surface initiated below the T_m of the bulk material;[1, 35] Chen and co-workers have also worked with free surfaces to determine T_m in polymers.[32] Importantly, both the point-defect

and surface methods show promise for mitigating superheating effects and delivering T_m closer to experimental measures.

We are interested in exploring the phase transitions of OSC developed from rigid, anthradithiophene (ADT) chromophores (Figure 1),[36-40] with a particular emphasis on understanding how the molecular structure and chemical substitution (here the alkylsilylethynyl functionalization approach that is often used to govern solubility) impact the molecular-scale features of the phase transitions. It is our aim to determine how these molecules transition from ordered to disordered phases during heating, and to look for hallmark characteristics that may lead to further insight into the crystal nucleation and growth in these and similar systems. Experimentally, ADT are challenging materials as they result in a 1:1 mixture of *syn* and *anti* configurations of the thiophene moieties during synthesis. The presence (or lack) of *syn* and *anti* ADT isomers in molecular materials has been shown to direct both the molecular order in the solid state and the resulting OSC characteristics, in particular the charge-carrier mobilities extracted from OFET architectures.

Here, we investigate the thermal transitions of the *syn* and *anti* isomers of both the ADT chromophore and 5,11-bis(triethylsilylethynyl) anthradithiophene (TES ADT). We demonstrate the impact of superheating in the MD simulations on the determination of T_m, and how the enhanced probability for disorder from both the void and interface methods can alter T_m. Interestingly, while the results for the unsubstituted ADT chromophores are clear cut, the impact of these different methods for the TES ADT derivatives is more nuanced. The descriptions of the molecular features associated with these thermal transitions provide distinctive insight into the how the chemistries of ADT-based materials direct their solid-state packing characteristics.

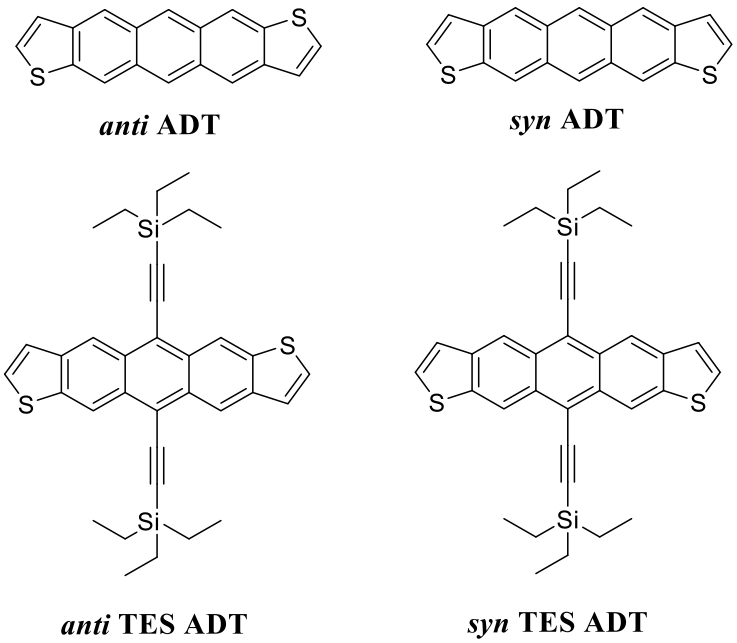

Figure 1. Chemical structures of the *anti* and *syn* isomers of [top] anthradithiophene (ADT) and [bottom] 5,11-bis(triethylsilylethynyl) anthradithiophene (TES ADT).

Computational Methodology

All MD simulations were performed using the GROMACS 2016.1 software package.[41, 42] The intra- and inter-molecular interaction parameters for the ADT molecules were built from the OPLS-AA (optimized potentials for liquid simulations – all atom) force field.[43, 44] Bonded force field parameters for the thiophene moiety were adapted from Schwarz and co-workers,[45] and those for the TES moiety were adapted from Do and co-workers.[46] All parameters were evaluated by comparing ADT energy minimized structures from molecular mechanics (MM) minimizations to molecular geometries optimized via density functional theory (DFT) at B3LYP/6-31G(d,p) level. Data from the comparisons are given in Tables S1 and S2 of the Supporting Information, and suggest that these OPLS-AA-based force field parameters provide molecular structures similar to the DFT optimized geometries.

To evaluate the nonbonding parameters, supercells created from the bulk crystal structure reported by Mamada and co-workers[47] containing 400 ADT molecules were subjected to MD simulation at 113 K and 1 bar, the temperature at which the crystal structure was obtained. Following an initial steepest descent energy minimization, these supercells were treated by one *NVT* (constant number, *N*, volume, *V*, temperature, *T*) and two *NPT* (number, *N*, pressure, *P*, temperature, *T*) steps using a leap-frog integrator with a 1 fs time step. Both *NPT* runs used a velocity rescaling thermostat[48] with a coupling time of 1.0 ps and a compressibility of 4.5×10^{-5} bar^{-1}. The first NPT step used the Berendsen[49] barostat, which is an efficient way to scale the system for initial equilibration yet produces artificially narrow distributions of pressure. The second *NPT* step used the Parrinello-Rahman[50] barostat for further equilibration. Three-dimensional PBC were applied and a spherical cut-off of 1.4 nm was used for van der Waals (vdW) interactions and particle-mesh Ewald (PME)[51] with 1.4 nm cutoff for long-range electrostatic interactions are used throughout the simulations. Each *NVT* and *NPT* simulation was carried out for 2 ns with the geometry from the second *NPT* ensemble used to generate crystal parameters for comparison with the experimentally derived parameters. Our results indicate that the nonbonding parameter applied for both the *anti* and *syn* ADT supercells effectively maintains the experimental crystal packing during the entire simulation time. The comparison of the experimental crystal parameters and the packing results derived from these MD simulations are provided in Table S3.

Potential of mean force (PMF) calculations, using constrained simulations, were performed *in vacuo* to determine the strength of the intermolecular interactions between the various ADT chemistries considered. For each PMF simulation, two ADT molecules were placed in a $10 \times 10 \times 10$ nm^3 simulation box. Two energy minimization processes (one of 1000 steps to remove potential overlap and one of 20,000 steps for minimization) were run for each sample window,

followed by an *NVT* simulation to equilibriate the system. An additional *NVT* simulation using a velocity rescaling thermostat with a coupling time of 2.0 ps was then run for data collection. The PBC were turned off and the cut-off was set to zero for the *in vacuo* simulations, and the production run was carried out at 298 K for 5 ns with a time step of 2 fs. The force data from the final 2 ns was averaged and the weighted histogram analysis method (WHAM)[52] in GROMACS was used to obtain the PMF profile.

To explore phase transformations during heating and eventual melting, supercells of the *anti* and *syn* ADT and *anti* and *syn* TES ADT crystals were created. The *anti* and *syn* ADT and *syn* TES ADT supercells included 1600 molecules, while the *anti* TES ADT supercell included 1350 molecules. These differences reflect the different number of molecules in each of the respective unit cells and a strategy to retain cube-like supercells. Thermal annealing simulations were carried out using a methodology similar to that employed by Palczynski and co-workers,[53] following a two-step protocol (Figure S2):

- The pre-equilibrium simulations were carried out with the method described above, with each *NVT* and *NPT* ensemble was carried out for 2 ns.
- Simulated annealing was performed using the final geometry of the previous step within the *NPT* ensemble using a Parrinello-Rahman barostat. Using a 2 fs time step, the system was heated linearly from 300 K at a rate of 60 K/ns until an isotropic melt was achieved. This was followed by additional heating to 1200 K at a rate of 40 K/ns with a 1 fs time step to achieve a gaseous state.

Since molecular diffusion rates change as a function of phase, the mean square displacement (MSD) was used to determine the crystalline melting point during simulated annealing. MSD is defined as

$$MSD = \langle (r - r_0)^2 \rangle = \frac{1}{N} \sum_{n=1}^{N} \left(r_n(t) - r_i(0) \right)^2$$

where $r_i(t)$ is the location of the center-of-mass (COM) of molecule *i* at time *t* and *N* is the total number of molecules in the system. Within a given phase, the molecular COM MSD varies linearly with time. A fitting procedure was applied to the unit phases and the intersection of these linear trends was assigned as the melting point.

Two additional supercell constructs were used to examine their impact on the processes and temperatures at which melting occurred in the simulations. The first was a supercell where voids were purposefully created by removing small groups of molecules.[34] A cluster of 12 molecules was defined as one void unit; this number was chosen so that each dimension of the void space was similar to the length of the ADT backbone, and that the overall shape of the void was cube-like, allowing the ADT molecules exposed to the void to freely move into the open space during heating. Each void was randomly inserted into the supercell. The overall void percentage was calculated based on the total number of molecules removed. Simulations for each void configuration were repeated 10 times to test the impacts of the random void placements on the melting temperature.

The second construct inserted a vacuum gap along select crystalline lattices to create surfaces (slabs). These structures were created using the *gmx editconf* and *gmx genconf* packages in GROMACS. Each of the void and slab constructs were subjected to the previously described MD

heating protocol. To maintain the gap configuration during initial *NPT* equilibrium stage of the slab calculations, a semi-isotropic coupling was used to turn off the pressure along *z* direction.

Results and Discussion

In the following, we begin with a brief description of the potential of mean force (PMF) simulations that were used to examine the strength of the intermolecular interactions of all ADT systems considered here. These results are then followed by those from the thermal annealing simulations of the bulk, void, and slab ADT structures. We then conclude with a description of the impact of the triethylsilylethynyl (TES) substitution on the ADT thermal transitions.

Intermolecular interactions via PMF simulations

The PMF simulations are used as a preliminary means to examine the impact of the molecular chemistry and symmetry on the strength of the intermolecular interactions (Figure 2). As expected, the intermoleuclar interactions are similar for both the ADT and TES ADT systems regardless of the symmetry of the thiophene groups (*syn* or *anti*) in the ADT core. For the unsubtituted ADT, the molecules begin to interact at an ≈1.5 nm (15 Å) COM distance. When the TES groups are added, the turn-on of the intermolecular interactions begins at ≈1.9 nm (19 Å), a function of the stronger dispersion interactions induced by the TES groups; these results confirm the importance of the trialkylsilylethynyl (TAS) groups on the packing of TAS-acene molecular materials.[54, 55] These distances will be of importance when the slab simulations are considered (*vida infra*). The potential energy minima arise at COM distances of approximately 0.4 nm for both sets of ADT, though the geometries differ whether or not that TES groups are considered. We note that at the PMF minima, the ADT COM are slightly smaller than those observed in the bulk crystal structures,

and that the interaction geometries differ from those found in the respective crystal structures, with the variation being larger for the TES ADT systems. These differences can be attributed to (i) effects that arise from many-body nature of the packing in the bulk crystals – in the PMF, the interactions only consider two molecules in vacuum – and (ii) intrinsic errors based on the deviations in the force field parameters to describe the systems.

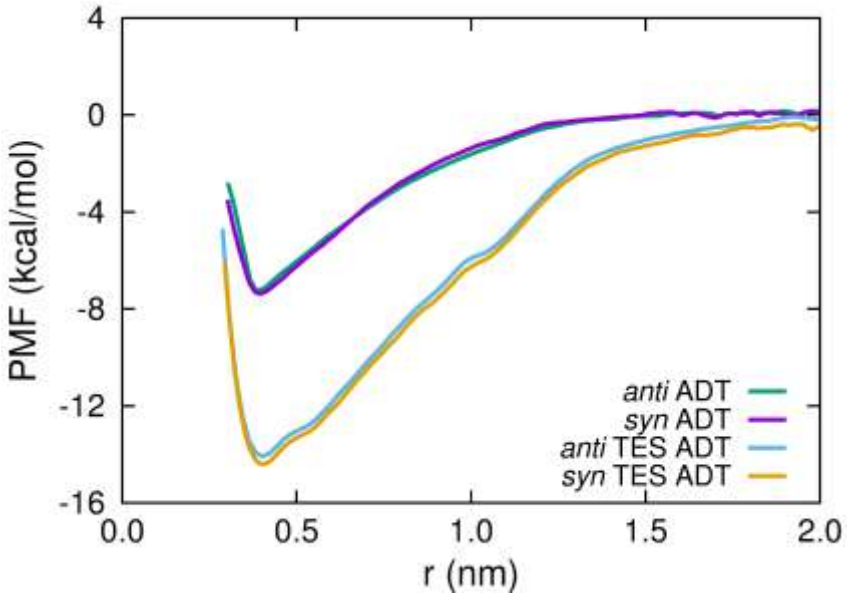

Figure 2. Potential of mean force (PMF) profiles of *anti* and *syn* ADT and TES ADT molecular pairs pulling along the axis perpendicular to the molecular planes.

ADT phase transformations during thermal annealing

Thermal annealing of bulk crystals. Among the more straightforward ways to determine the melting temperature (T_m) of bulk, periodic systems from simulations is via density *vs.* temperature plots (Figure 3), where discontinuities in the density indicate a phase change or some manner of molecular rearrangement. The heat capacity at constant pressure (C_p) *vs.* temperature also serves as an efficient indicator of phase change since sharp peaks indicate exothermic or endothermic processes. Notably, C_p sharply peaks at discontinuities in the density plots, providing another identification of T_m. Finally, we use the total energy of the system to identify first-order transitions

(Figure 4). Melting transitions are identified as sharp discontinuities in the total system energy (sum of the potential and kinetic energies) *vs.* temperature plots. The simulated T_m was identified as the temperature at the center of the discontinuity.

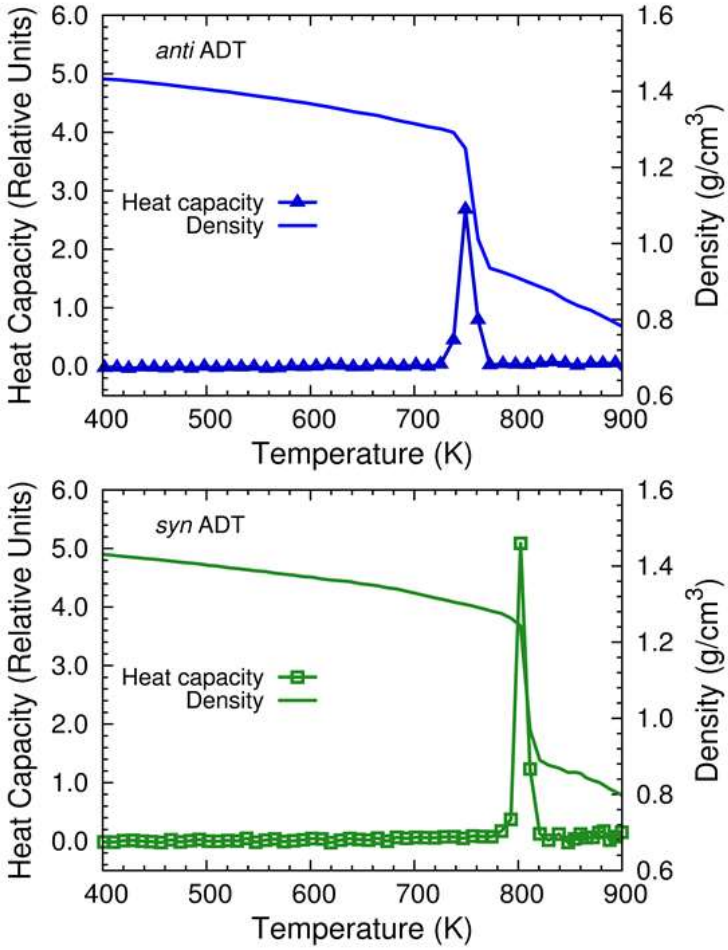

Figure 3. Density *vs.* temperature and heat capacity (C_p) *vs.* temperature plots for [top] *anti* and [bottom] *syn* ADT bulk crystals.

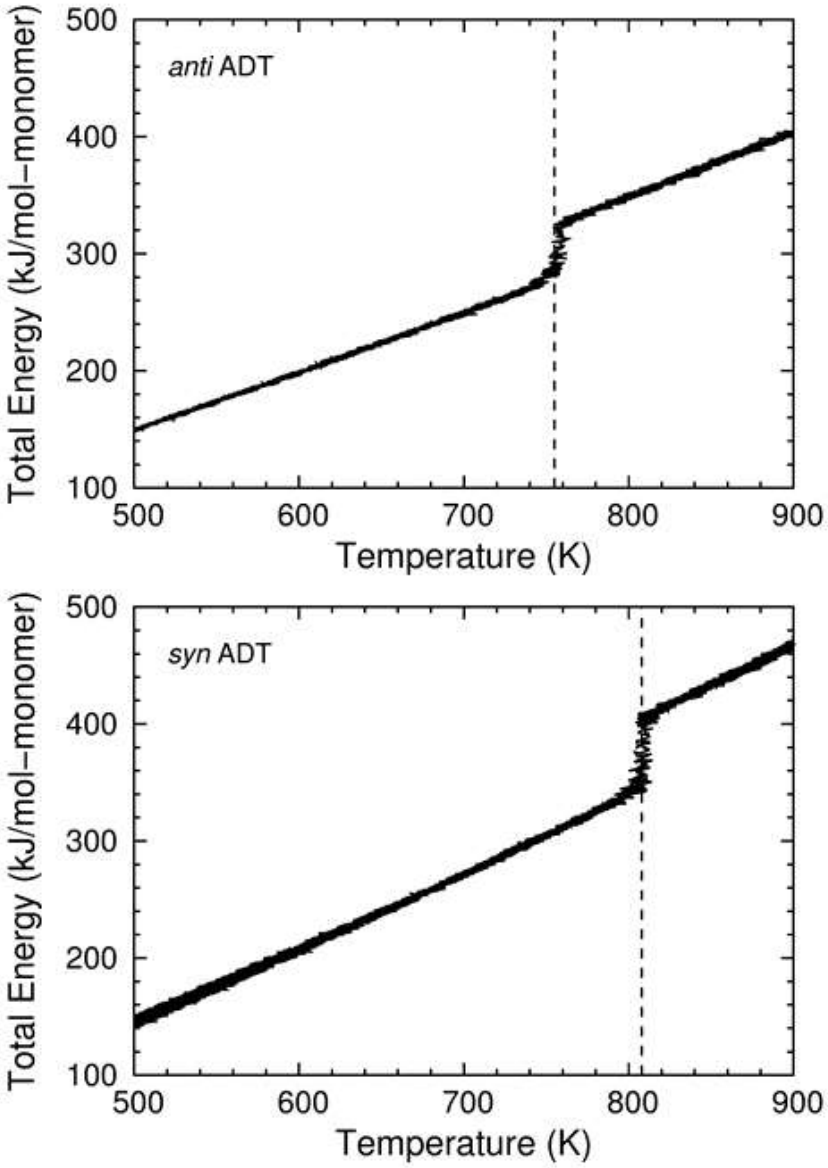

Figure 4. Total energy profiles for [top] *anti* and [bottom] *syn* ADT crystals during thermal annealing.

From the density *vs.* temperature and energy *vs.* temperature analyses of the bulk, periodic structures, the simulated T_m of *anti* and *syn* ADT are estimated to be 750 K and 808 K, respectively. Differential scanning calorimetry (DSC) experiments[47] provide T_m for *anti* and *syn* ADT of 725 K and 720 K, respectively. Hence, these bulk simulations overestimate T_m by 25 K and 83 K,

respectively. It is notable that the solid-liquid (SL) phase transitions occur over short temperature ranges in the simulations, shown as sudden discontinuities in the density *vs.* temperature and total energy *vs.* temperature plots or as sharp peaks in the heat capacity *vs.* temperature plots. Such sharp peaks, in part, can be assigned to the fact that the simulated heating took place equally throughout the entire simulation box, which is unlike experiments where melting might be expected to first occur on the materials surface. Overall, these results demonstrate qualitative and quantitative failures that arise from spurious superheating due to the simulation constraints.

Thermal annealing of bulk crystals with voids. The T_m derived using the fully periodic systems are clearly too large. Hence, it is important to evaluate if different methods can allow for more representative descriptions. To explore alternative methods, we begin with the so-called void method, where groups of molecules are removed from the bulk structure.[34] There are a number of considerations that need to be made when implementing this method. It is important to note that the ADT molecules are essentially rigid rods packed in tight configurations (density = 1.53 g/cm^3). Hence, if only single, isolated molecules are removed from the system, the neighboring molecules can readily occupy the resulting voids through only small translations or rotations during equilibration. Here, such defects are not sufficient to modify the T_m significantly from the periodic bulk simulations, unless many voids are created. An additional requirement for these simulations is that a sufficient amount of the crystal must be kept to maintain the integrity of the crystal structure; if too many voids are introduced, the crystal becomes mechanically unstable and collapses without the hallmark discontinuity expected for SL phase transitions.[56-58]

Instead of removing only a single molecule from many points in the supercell, we removed small groups consisting of 12 molecules to create the voids. In this case, the ADT molecules exposed to the void can move more freely, and over larger distances, into the open space during heating. The

total void percentage was calculated according to the total number of molecules removed from the system. We randomly made 10 configurations for each void percentage to generate data for statistical analyses. A pictorial comparison of the resulting void systems made by removing either a one molecule or 12 molecule unit is shown in Figure S3.

The relative MSD as a function of the annealing temperature for the (12 molecule) void systems are given in Figure S4. T_m is interpreted by the points of intersection found for two linear fits in different regions of the curves. Overall, the results from the void simulations follow the trends established by the fully periodic bulk calculations, though the T_m in general decrease. With 2% voids, $T_m$decreases from 775 K (bulk) to 752 K for *anti* ADT and 804 K (bulk) to 753 K for *syn* ADT. As the number of voids increases, the shifts of the MSD profiles become less pronounced. From 10-30 % voids, the calculated T_m is independent to the number of voids, as show in Figure 6. The temperature corresponding to this plateau region is taken to be the T_m of the unsubstituted ADT, and are estimated at 720 K for *anti* ADT and 710 K for *syn* ADT. While there is still a 10 K to 20 K variation in T_m, these results are qualitatively more consistent with experiment with respct to the PBC simulations, and provide insight into the impact of increased disorder in ADT materials upon heating. A series of snapshots (Figure 5) from the void simulations reveal that the voids allow larger degrees of translational and rotational freedom when compared to the bulk simulations, with adjacent molecules filling the void space during the annealing process. It is this additional freedom of motion that allows for the simulated T_m to come more in line with experiment.

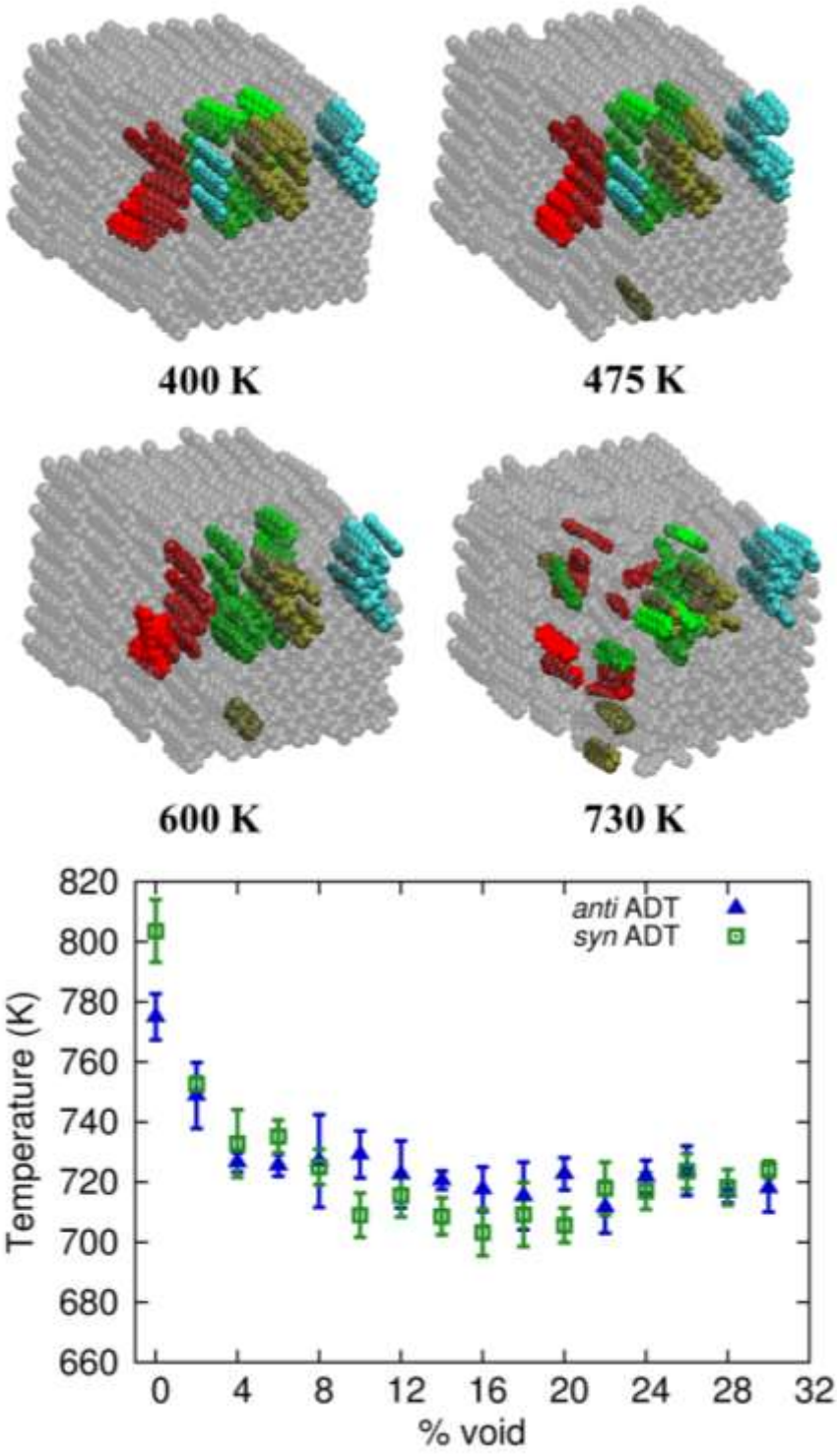

Figure 5. [top] Snapshots from one of the *anti* ADT systems with 14 % voids shows the melting process from 400 K to 730 K. [bottom] Melting point as function of void percentage determined from the MSD.

Thermal annealing of slabs. While the defects induced in the void systems lead to better agreement with the experimental T_m, one may question how such a system relates to those used in DSC experiments. During DSC, for instance, there are definite free/exposed surfaces that will first encounter the heat applied during the experiment. To examine such a consequence, a series of periodic structures were created in which a vacuum gap was installed along explicit crystallographic planes to create slabs – here, the (001), (100), and (010) crystal faces – and these structures were then used in the thermal annealing simulations (Figure S5).

As shown in Figure 6, the (001) slabs present similar C_p profiles as the fully periodic ADTs, while the (100) and (010) slabs show significantly decreased C_p peak temperatures and T_m. For both *anti* and *syn* ADT, the (010) slab presents a T_m around 700 K, which is in close agreement with experiment. For the (010) slab, the molecules lie with their long axes parallel to the surface, with the molecules underneath arranged in a herringbone packing configuration. Hence, each molecule on the surface is only held in place by relatively weak C–H•••π noncovalent interactions that are readily overcome upon heating. Figure 6 depicts the melting process at this surface: As the temperature increases, thermally induced translational and rotational modes become more active. These modes eventually lead to the surface molecules breaking away to enter the vacuum gap, while the lower layers of the bulk-like molecules maintain the crystal packing. Further heating leads to the remaining molecules in the solid melting, and eventually the full liquid state being formed. The temperature range of this entire process covers about 100 K, as is represented as the broad peak in the heat capacity profile.

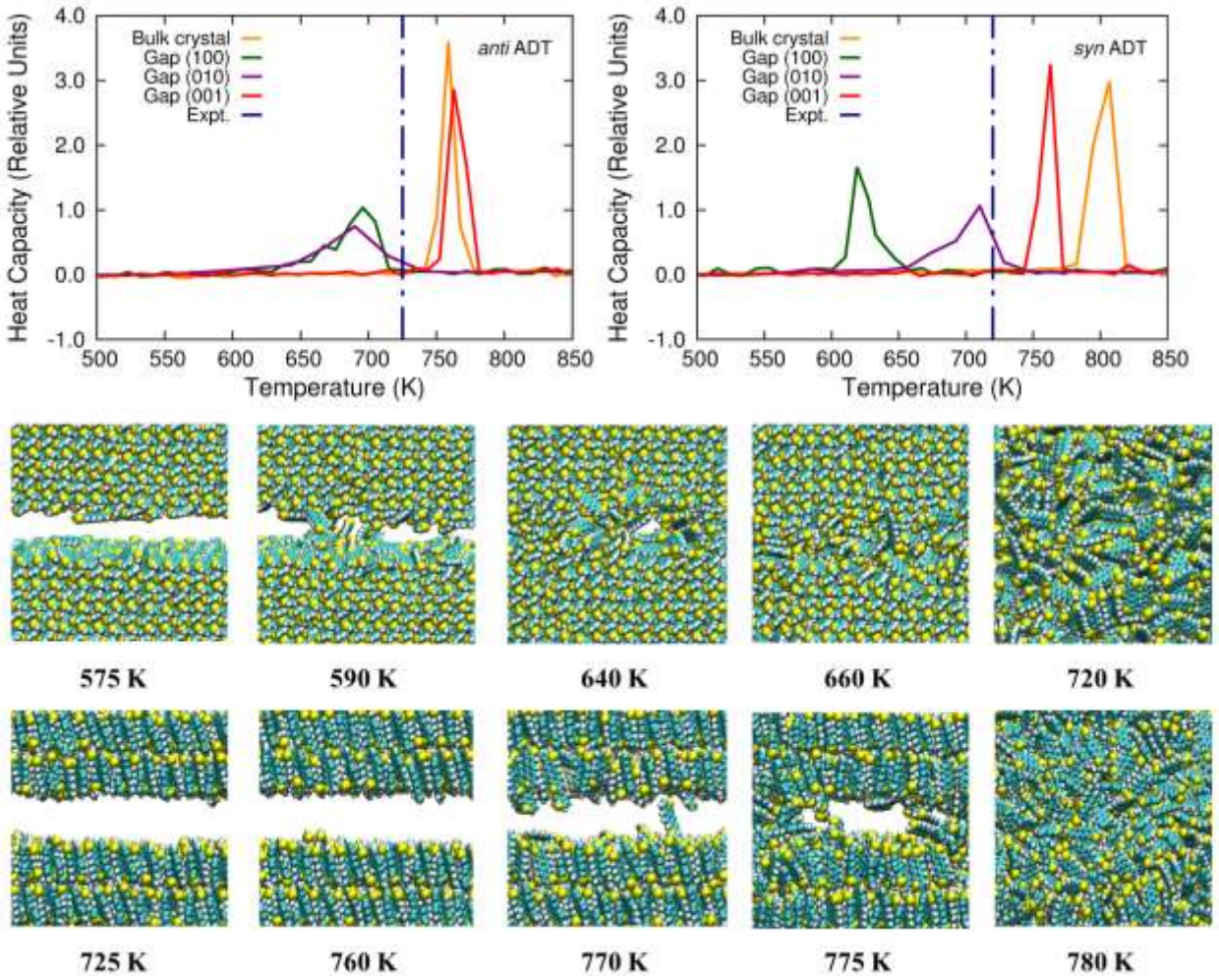

Figure 6. [top] Change of heat capacity as a function of temperature of bulk crystals and various slab structures. [bottom] Snapshots of *anti* ADT with gaps along the (010) (upper structures) and (001) (bottom structures) surfaces taken at different temperatures during the annealing process. Note that while the (010) slab structure is fully melted at 720 K, the (001) structure remains quite ordered at higher temperatures.

On the contrary, the (001) slab exposes the ADT short axis. Now, to escape the solid state, the molecules need to overcome intermolecular interactions that cover a larger portion of the molecular volume. As shown in Figure 6, even at 720 K where the (010) structure is melted, the top molecular layer of the (001) slab maintains a crystal-like packing. It is only as the temperature keeps increasing from 725 K to 770 K that the molecules in this slab eventually escape the solid.

Once a few molecules do enter the gap, the system breaks apart rapidly, and at 780 K the entire system is in the liquid state. This process is represented by a sharp peak in the heat capacity profile, which is similar to that observed from the simulations on bulk crystal. More snapshots of each slab system may be found in the Supporting Information (Figures S6 and S7).

For these slab structures, plots of the system total energy *vs.* temperature reveal additional insight pertaining to the phase transitions (Figure 7). The T_m (onset of melting) and T_{end} (fully melted) can be acquired from the plots, which appear to be composed of three sections: (i) a linear region with where the energy increases with temperature followed by (ii) a roughly quadratic rise in the energy that is followed by (iii) a second linear rise in energy with increasing temperature. The onset of T_m was determined from the regression analysis method used by Chen and co-workers:[32] Sections (i) and (iii) were fit with linear functions, while part (ii) was fit with a constrained quadratic function. Notably, the width of each parabola can be related with a force constant that represents the force required to move the molecules from the surface into the gap. The wider parabolic curves for the (100) and (010) surfaces arise from smaller coefficients in the quadratic functions, suggesting a small force constant for melting, while the narrower quadratic curve for the (001) slab indicates that a larger force is required to extract the molecules from the solid. In general, the melting along the various slabs differs rather dramatically, as one might expect given the very different intermolecular interactions at play on each surface. We note that this conclusion diverges from that of Chen and co-workers for isotatic polypropylene,[32] but makes physical sense given the anisotropic nature of the ADT.

We do note that the T_m derived from the total energy *vs.* temperature plots differ from those derived from the C_p *vs.* temperature plots. This variation is due to how the T_m are assigned: In the C_p plots, sharp peaks are used to identify T_m, while in the total energy plots, the T_m was defined

as the "onset of melting", while the T_{end} represents the temperature when system is fully melted. Here, the onset of melting commences when the surface molecules being to migrate into the gap, though the majority of the systems remain crystal-like.

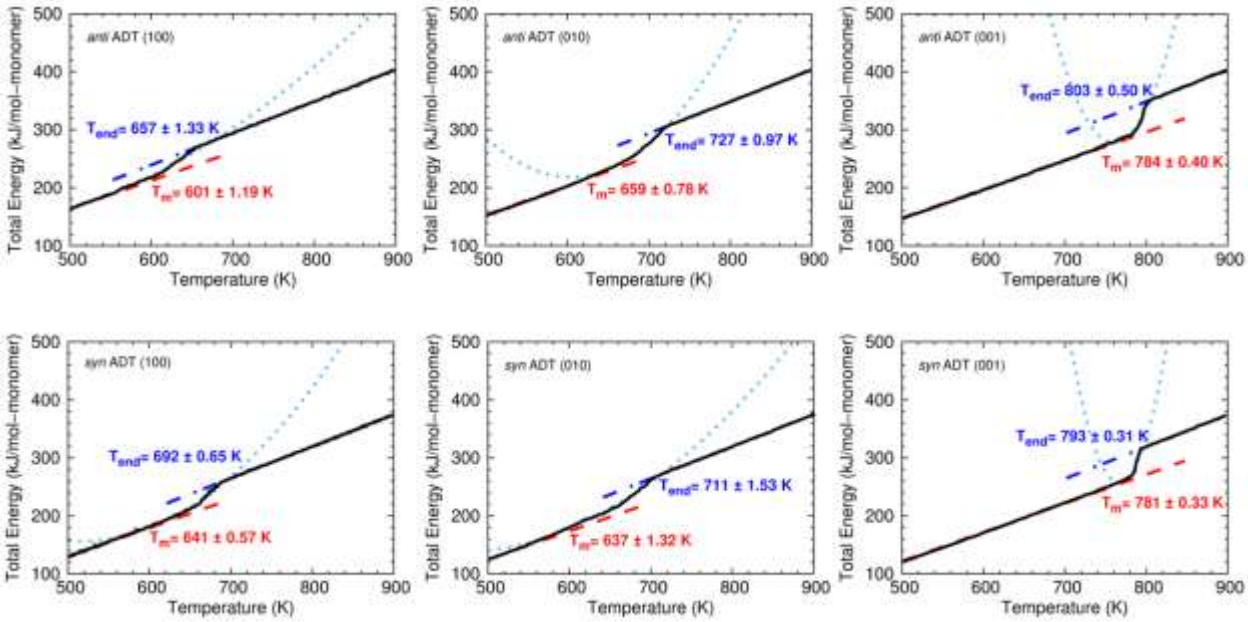

Figure 7. Total energy *vs.* temperature profiles for *anti* and *syn* ADT slab systems.

For the slab systems, an additional aspect to consider is whether the width of the vacuum layer is large enough to prevent intermolecular forces acting across the gap to influence the melting, and how different gap widths influence the determination of T_m; ideally, T_m should be independent of the gap size. To explore this feature, a series of *anti* and *syn* ADT systems with different gap widths were created for the (010) surface and the same melting approach was applied. Figure S8 shows T_m as a function of the gap width, which decreases with increasing gap width up to a critical point at 15 Å, after which no further change in T_m is observed with increasing gap width. This in part can be explained by the PMF simulations, which show that the intermolecular interactions become very weak to nonexistent for ADT at approximately 15 Å – *i.e.* this is the point at which molecules

on the two different surfaces that form the gap no longer "feel" each other. It is also notable that to maintain the gap during initial equilibrium step, a sufficient gap width is required to overcome the interaction between two building blocks across the vacuum (see Figure S9).

Thermal annealing of the anti and syn TES ADT systems.

We now turn to the TES ADT systems. Here, it is important to recall two important distinctions: (i) the ADT now contain the triethylsilylethynyl (TES) arms that are appended to enhance solubility and (ii) these groups change the ADT herringbone packing configuration to one that is brickwork for *anti* TES ADT[59, 60] or a one that adopts a monoclinic lattice with two molecules per unit cell for *syn* TES ADT.[61] Starting with the bulk thermal annealing approach as applied to *anti* and *syn* ADT bulk crystals, the change in C_p as function of temperature for both *anti* and *syn* TES ADT exhibit small peaks prior to reaching the melting point, which corresponds with discontinuities in the respective density *vs.* temperature profiles (Figure 8). Deeper inspection reveals a solid-solid (SS) phase transition, wherein the molecules reorient. In *anti* TES ADT, the original crystal at 100 K has a brickwork packing configuration, and the SS phase transition can be described by a change in the angle formed between the ADT backbone and *z*-direction (defined in Figure 9), which changes from 70° to 100° in the temperature range from 400 K to 518 K. At 518 K, all molecules in the bulk crystal are aligned in a new brickwork-like orientation, which is maintained until 850 K when the solid melts.

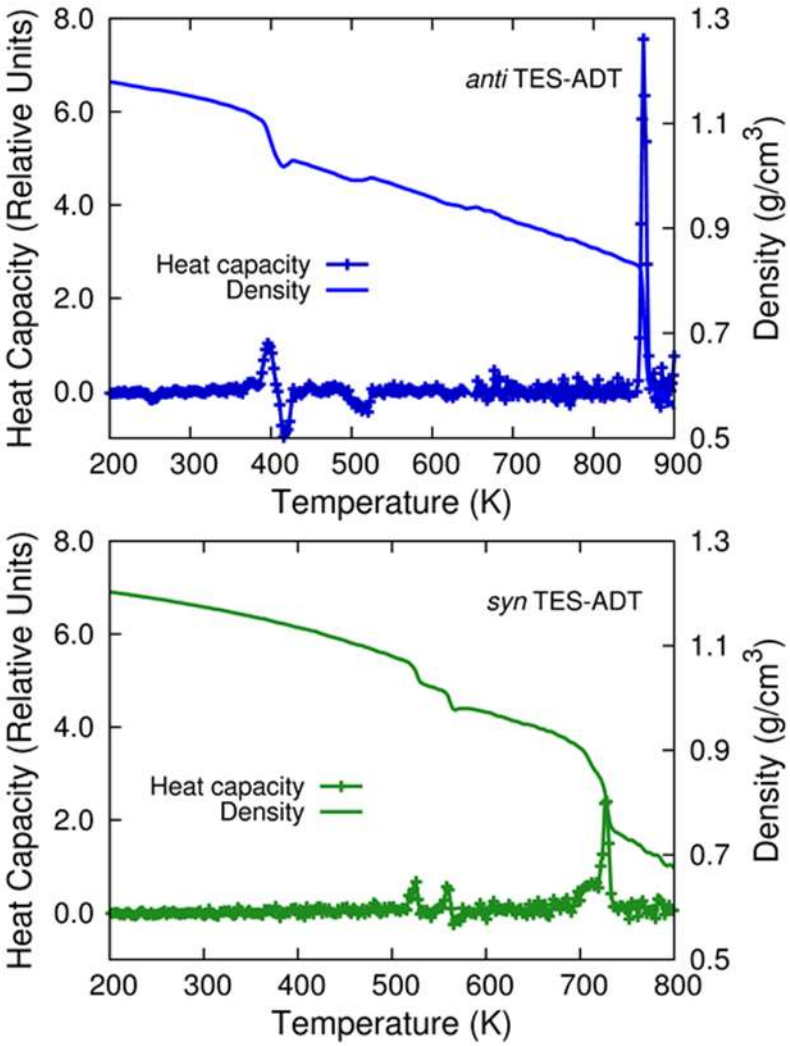

Figure 8. Density and heat capacity as function of temperature of [top] *anti* and [bottom] *syn* TES ADT bulk crystals.

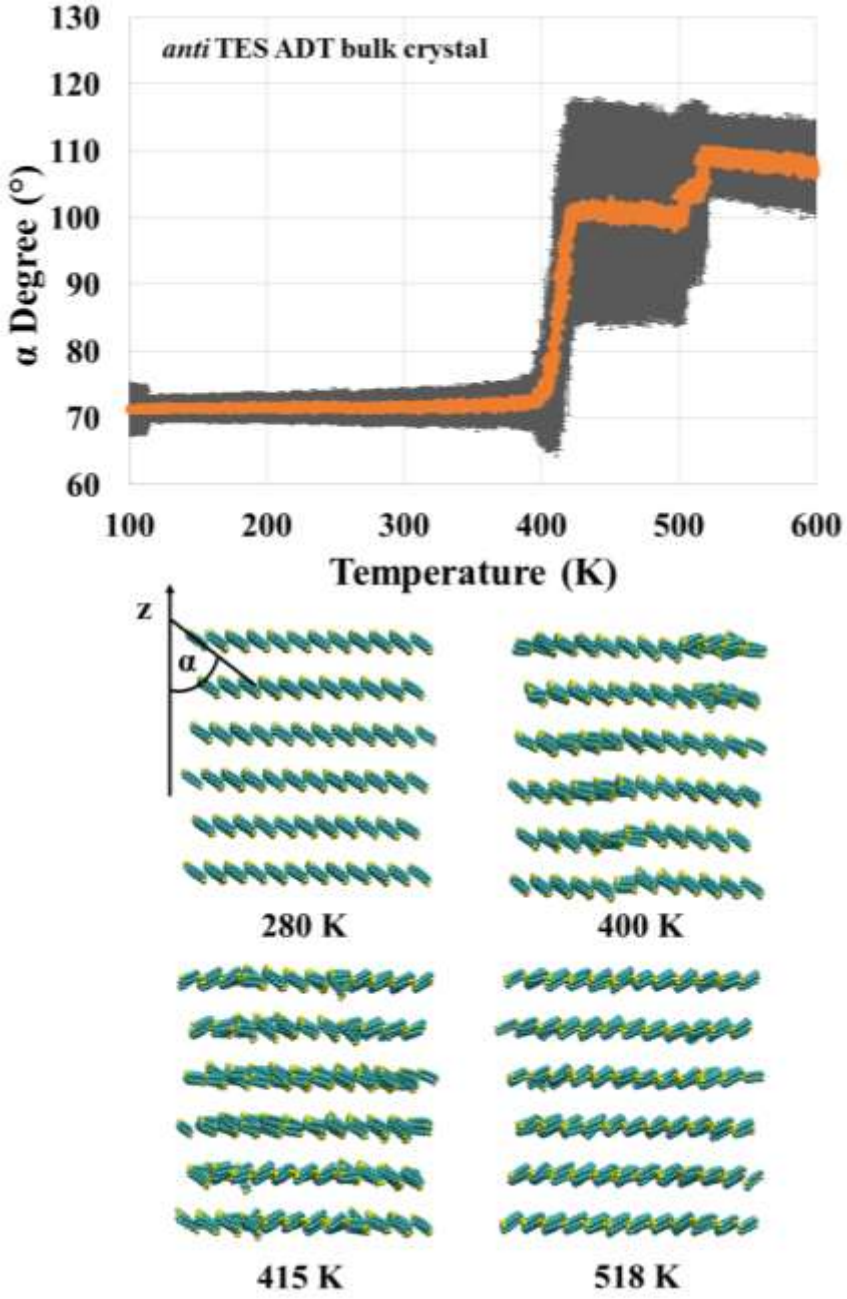

Figure 9. [Top] Change in angle between the *anti* TES ADT backbone and the *z*-direction as a function of temperature. [Bottom] Snapshots of the *anti* TES ADT bulk crystal during thermal annealing to demonstrate the reorientation of ADT backbone.

To investigate further the nature of the SS transitions of *anti* TES ADT during thermal annealing, powder x-ray diffraction (XRD) spectra were simulated at select temperatures along the thermal

trajectory (Figure 10); the simulated XRD spectra were determined with the Mercury 3.6 software suite[62-65] using a wavelength of 1.033 Å. From these powder XRD simulations, four distinct structures were identified: (i) The initial, bulk crystal structure was maintained at two lower temperatures (100 K and 280 K), with two ordered, yet different packing configurations observed at (ii) 415 K and (iii) 518 K, and finally (iv) the fully melted, liquid phase at 870 K. Notably, previous DSC experiments have shown the existence of varied packing configurations in TES ADT:[66] three crystalline structures (denoted α, β, and γ) and an amorphous phase (denoted the *a* phase). Comparison of the wide-angle x-ray scattering (WAXS) patterns reported in Reference 66 with our simulated powder XRD spectra reveal generally good agreement. The structures reported here at 100 K and 280 K can be identified with the α phase (the as-cast phase developed at room temperature), while the simulated XRD pattern developed for the 415 K structure closely resembles the γ phase. The simulated XRD pattern for the structure at 518 K shares similar features with the β phase, which was observed during the first heating cycle of TES ADT thin film; here, there is a distinct peak at 0.6 $Å^{-1}$ and a set of narrow peaks that range from 0.75 $Å^{-1}$ to 1.25 $Å^{-1}$ that are not observed in the other packing configurations in both the simulations and experiment. Finally, the amorphous a phase is the featureless simulated XRD pattern at 800 K. We do note that the agreement is not perfect, though there are enough features to provide confidence in the assignments.

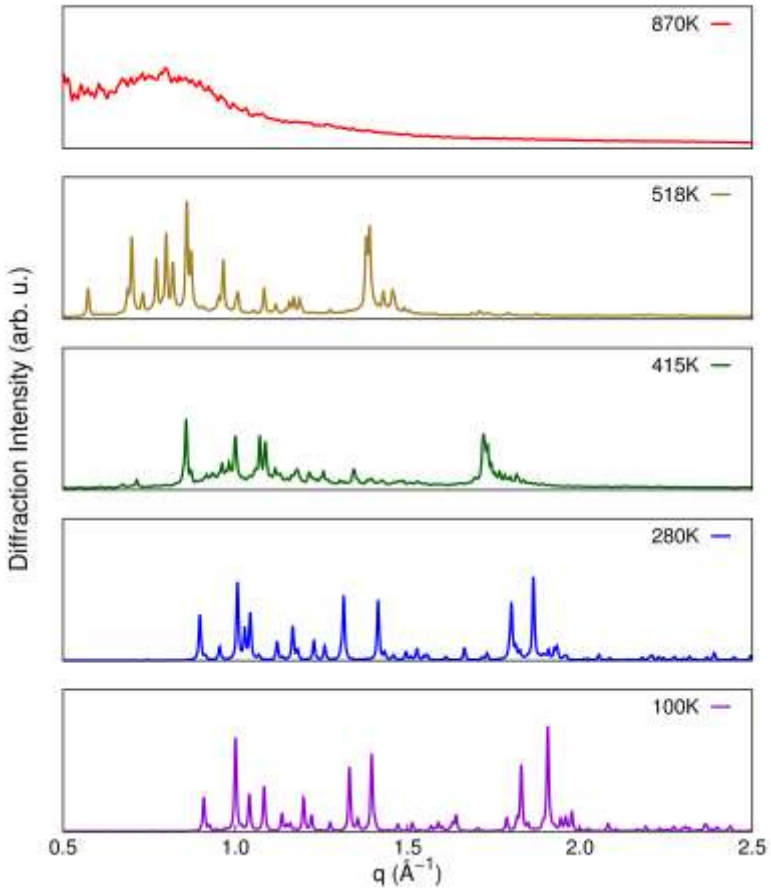

Figure 10. Simulated temperature-dependent XRD spectra for *anti* TES ADT. The temperatures, from bottom-to-top, are 100 K, 280 K, 415 K, 518 K, and 870 K.

Turning to *syn* TES ADT, a similar molecular reorientation is observed upon heating. The unit cell of *syn* TES ADT contains two molecules, with an angle between two molecular planes of 42°. As the temperature increases, the angle between the two molecules decreases and both molecules change their orientation to a more brickwork packing, as shown in Figure 11. Unlike the *anti* TES ADT reorientation, which occurs for all the molecules before melting, the reorientation in *syn* TES ADT occurs in only a portion of the bulk crystal, while different regions of the crystal undergo a

simple increase in disorder and melting. As the temperature continues to increase, these disordered regions act as seeds that expand to melt the entire crystal.

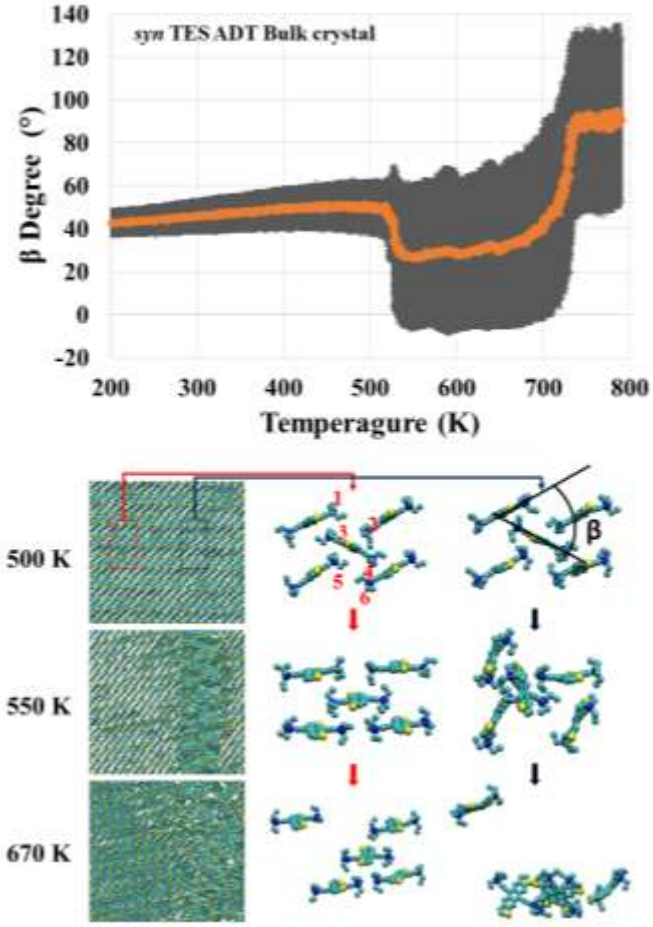

Figure 11. [Top] Change in angle between the backbone planes of two *syn* TES ADT as a function of annealing temperature. [Bottom] Snapshots of two parts of the *syn* TES ADT bulk crystal during thermal annealing process.

Moving to slab simulations, the *anti* TES ADT slabs show similar transitions in the heat capacity profiles, indicating that the molecules reorient in a like fashion for all surfaces considered (Figure 12). For the (100) and (010) slabs, the ADT backbone is more exposed, leading to a decrease in T_m compared with the bulk crystal. The (001) slab has the TES side group exposed, and this surface

shows a similar heating profile with the bulk crystal. The reported melting point for *anti* TES ADT is around 405 K,[61] which is much lower than the simulated melting range in all systems; however, this melting point falls within the reorientation temperature range noted above, suggesting there may be connections between the experimental melting process and reorientation seen in the simulations. (Figure S10).

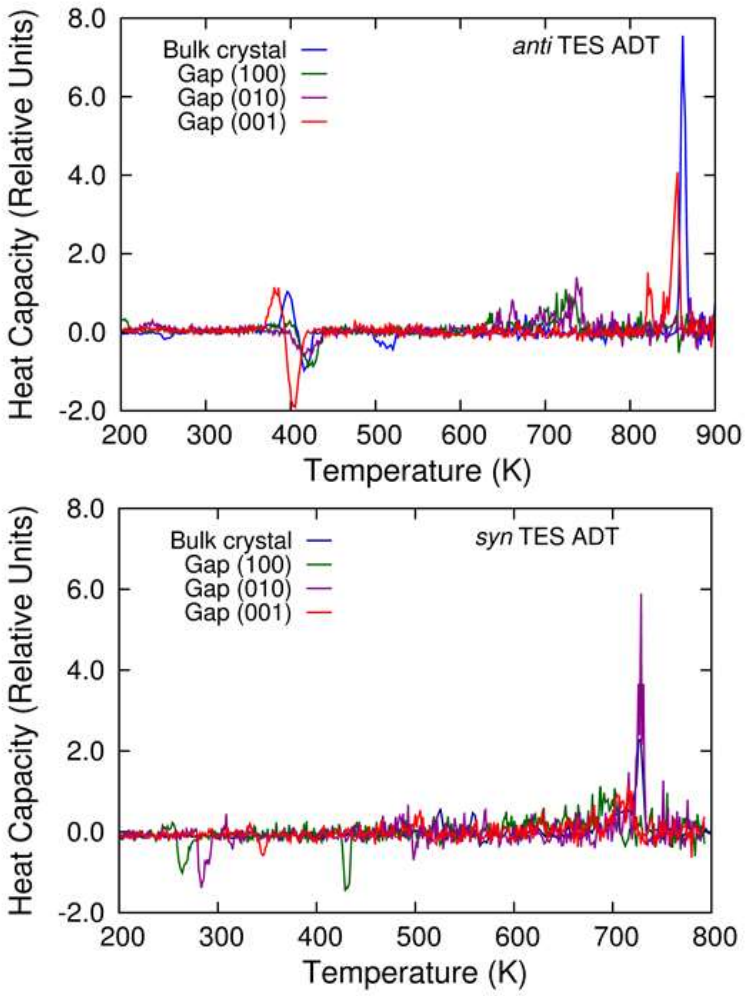

Figure 12. Change of heat capacity as a function of temperature of for [top] *anti* and [bottom] *syn* TES ADT bulk crystals and crystals with gaps along different surfaces.

The *syn* TES ADT slab systems exhibit distinct thermal ranges in terms of molecular reorientation events. Particularly, the (100) surface exhibits an additional peak at 430 K. Deeper analysis of the angle distributions between the two molecules in the same unit cells reveals that the (100) slabs go through two steps to form the final brickwork like packing feature: At 270 K, the angle between two molecules decreases from 38 ± 4° to 26 ± 16°, and this configuration is maintained until 430 K, where the angle further decreases to 16 ± 9° until the system starts to melt at 580 K (Figure S11). The (001) slab system exhibits the lowest melting temperature at 510 K, which is still significantly larger than the experimental melting temperature at 390 K. From these results, it is hypothesized that disorder in the experimental *syn* TES ADT sample also contributes to the lower melting temperature. Additional snapshots of the *syn* TES ADT slabs showing the reorientation during annealing process can be found in Figure S12.

The reorientation of the *syn* TES ADT systems during thermal annealing can also be determined through the radial distribution functions (RDF) of Si-Si pairs among molecules in different layers. As shown in Figure S13, the peak at 0.7 nm represents the Si-Si distance between two adjacent layers, which as the temperature increases, decreases from 0.7 nm to around 0.5 nm (Pair: 1-2). This change indicates a reorientation of two layers from a monoclinic lattice[61] to a head-to-tail configuration. Another significant change of the RDF is the peak at 1.4 nm, corresponding to the long Si-Si distance between two molecules in the same unit cell, which shifts from 1.4 nm to 1.0 nm. This shift indicates that the reorientation of the molecules in the unit cell changes from edge-to-face to a brick-work configuration. More snapshots of each slab system at different temperatures during thermal annealing are available in the SI.

Conclusion

Thermoanalytical techniques offer distinctive capabilities to employ a macroscopic measurement to understand how molecular-scale features impact the solid-state packing of OSC. Further insight can be derived through atomistic MD simulations, provided that the simulations deliver results that are in line with experiment. Here we explore the phase transitions upon the heating of *anti* and *syn* ADT and TES ADT derivatives. Simulations of the melting process using PBC bulk crystals show strong superheating effects, with the effect more significant for the TES ADT molecules. Providing free space for molecules to move and the opportunity for increased disorder – either through the introduction of voids into the supercell or the creation of free surfaces – reduces superheating effects rather dramatically. For the *anti* and *syn* ADT systems, a small number of voids accelerates the melting process, and can result in good agreement with experimentally determined T_m. The slab systems show a strong dependence of T_m with respect to the exposed surface, which is a consequence of the molecular anisotropy. Again, good agreement with experiment can be obtained with the slab simulations, with these models providing opportunities to mimic the melting processes expected in these crystals. For the TES ADT molecules, the free surfaces had minimal effect on accelerating the melting process, with the T_m derived for all exposed surfaces being similar to the bulk crystals. However, distinct SS transformations were observed for the TES ADT systems, with the temperature range for these transitions similar to the reported T_m. Investigation of the molecular packing configurations reveals significant TES ADT reorientions during these SS transitions.

Notably, the atomic-level details pertaining to the nature of the phase transitions in these ADT-based materials provide critical information as to how changes in chemical structure impact molecular motion during annealing. Such information pertaining to how the molecules move and

disperse upon heating can be correlated with expectations as to how changes in molecular chemistry may affect the nucleation and growth of these materials. Simulations are currently ongoing into the nucleation and growth of these systems in order to demonstrate the robustness of these correlations, with the goal of increasing the knowledge required to rationally engineer OSC crystal packing.

Acknowledgements

This work was supported in part by the National Science Foundation (Award No. CMMI 1563412) and the Office of Naval Research (Award No. N00014-16-1-2985). Supercomputing resources on the Lipscomb High Performance Computing Cluster were provided by the University of Kentucky Information Technology Department and Center for Computational Sciences (CCS), and on the Holly computing cluster by the University of Kentucky College of Arts & Sciences.

References

1. N. Takahashi, M. Hikosaka and T. Yamamoto, *Phys. B*, 1996, **219-220**, 420-422.
2. S. A. Arnstein and C. D. Sherrill, *Phys. Chem. Chem. Phys.*, 2008, **10**, 2646-2655.
3. S. Tsuzuki, K. Honda and R. Azumi, *J. Am. Chem. Soc.*, 2002, **124**, 12200-12209.
4. E. G. Hohenstein and C. D. Sherrill, *J. Phys. Chem. A*, 2009, **113**, 878-886.
5. E. G. Hohenstein, J. Duan and C. D. Sherrill, *J. Am. Chem. Soc.*, 2011, **133**, 13244-13247.
6. S. E. Wheeler and J. W. Bloom, *Chem. Commun.*, 2014, **50**, 11118-11121.
7. C. Sutton, C. Risko and J.-L. Brédas, *Chem. Mater.*, 2016, **28**, 3-16.
8. K. J. Thorley and C. Risko, *J. Mater. Chem. C*, 2016, **4**, 4040-4048.
9. G. Gryn'ova and C. Corminboeuf, *J. Phys. Chem. Lett.*, 2018, **9**, 2298-2304.
10. B. Jeziorski, R. Moszynski and K. Szalewicz, *Chem. Rev.*, 1994, **94**, 1887-1930.
11. M. O. Sinnokrot and C. D. Sherrill, *J. Phys. Chem. A*, 2004, **108**, 10200-10207.
12. M. O. Sinnokrot and C. D. Sherrill, *J. Am. Chem. Soc.*, 2004, **126**, 7690-7697.
13. R. Podeszwa, R. Bukowski and K. Szalewicz, *J. Phys. Chem. A*, 2006, **110**, 10345-10354.
14. A. L. Ringer, M. S. Figgs, M. O. Sinnokrot and C. D. Sherrill, *J. Phys. Chem. A*, 2006, **110**, 10822-10828.

15. M. O. Sinnokrot and C. D. Sherrill, *J. Phys. Chem. A*, 2006, **110**, 10656-10668.
16. R. Podeszwa and K. Szalewicz, *Phys. Chem. Chem. Phys.*, 2008, **10**, 2735-2746.
17. S. E. Wheeler and K. N. Houk, *J. Am. Chem. Soc.*, 2008, **130**, 10854-10855.
18. S. E. Wheeler, A. J. McNeil, P. Müller, T. M. Swager and K. N. Houk, *J. Am. Chem. Soc.*, 2010, **132**, 3304-3311.
19. S. E. Wheeler, *Acc. Chem. Res.*, 2013, **46**, 1029-1038.
20. S. Kirkland-York, K. Gallow, J. Ray, Y.-l. Loob and C. McCormick, *Soft Matter*, 2009, **5**, 2179-2182
21. B. S. Beckingham, V. Ho and R. A. Segalman, *Macromolecules*, 2014, **47**, 8305-8310.
22. N. D. Treat, P. Westacott and N. Stingelin, *Annu. Rev. Mater. Res.*, 2015, **45**, 459-490.
23. L. Yu, E. Davidson, A. Sharma, M. R. Andersson, R. Segalman and C. Muller, *Chem. Mater.*, 2017, **29**, 5654-5662.
24. H. Heinz, R. A. Vaia and B. L. Farmer, *Langmuir*, 2008, **24**, 3727-3733.
25. L. W. Antony, N. E. Jackson, I. Lyubimov, V. Vishwanath, M. D. Ediger and J. J. de Pablo, *ACS Cent. Sci.*, 2017, **3**, 415-424.
26. S. E. Root, N. E. Jackson, S. Savagatrup, G. Arya and D. J. Lipomi, *Energy Environ. Sci.*, 2017, **10**, 558-569.
27. A. Soldera, *Maromol. Symp.*, 1998, **133**, 21-32.
28. S. W. Watt, J. A. Chisholm, W. Jones and S. Motherwell, *J. Chem. Phys.*, 2004, **121**, 9565-9573.
29. S. E. Root, S. Savagatrup, A. D. Printz, D. Rodriquez and D. J. Lipomi, *Chem. Rev.*, 2017, **117**, 6467-6499.
30. K. Lu and Y. Li, *Phys. Rev. Lett.*, 1998, **80**, 4474-4477.
31. S.-N. Luo and T. J. Ahrens, *Appl. Phys. Lett.*, 2003, **82**, 1836-1838.
32. Q. Chen, E. B. Sirota, M. Zhang, T. C. M. Chung and S. T. Milner, *Macromolecules*, 2015, **48**, 8885-8896.
33. G. F. Velardez, S. Alavi and D. L. Thompson, *J. Chem. Phys.*, 2004, **120**, 9151-9159.
34. S. Jayaraman and E. J. Maginn, *J. Chem. Phys.*, 2007, **127**, 214504.
35. N. Takahashi, T. Yamamoto and M. Hikosaka, *Prog. Theor. Phys. Suppl.*, 2000, **138**, 414-415.
36. J. G. Laquindanum, H. E. Katz and A. J. Lovinger, *J. Am. Chem. Soc.*, 1998, **120**, 664-672.
37. M. M. Payne, S. A. Odom, S. R. Parkin and J. E. Anthony, *Org. Lett.*, 2004, **6**, 3325-3328.
38. M. M. Payne, S. R. Parkin, J. E. Anthony, C.-C. Kuo and T. N. Jackson, *J. Am. Chem. Soc*, 2005, **127**, 4986-4987.
39. D. Lehnherr and R. R. Tykwinski, *Aust. J. Chem.*, 2011, **64**, 919-929.
40. D. Lehnherr, A. R. Waterloo, K. P. Goetz, M. M. Payne, F. Hampel, J. E. Anthony, O. D. Jurchescu and R. R. Tykwinski, *Org. Lett.*, 2012, **14**, 3660–3663.
41. H. J. C. Berendsen, D. Vanderspoel and R. Vandrunen, *Comput. Phys. Commun.*, 1995, **91**, 43-56.
42. B. Hess, C. Kutzner, D. v. d. Spoel and E. Lindahl, *J. Chem. Theory Comput.*, 2008, **4**, 435-447.
43. C. E. Bernardes and A. Joseph, *J. Phys. Chem. A*, 2015, **119**, 3023-3034.
44. D. S. M. William L. Jorgensen, and Julian Tirado-Rives, *J. Am. Chem. Soc.*, 1996, **118**, 11225-11236.
45. K. N. Schwarz, T. W. Kee and D. M. Huang, *Nanoscale*, 2013, **5**, 2017-2027.

46. K. Do, C. Risko, J. E. Anthony, A. Amassian and J.-L. Brédas, *Chem. Mater.*, 2015, **27**, 7643-7651.
47. M. Mamada, H. Katagiri, M. Mizukami, K. Honda, T. Minamiki, R. Teraoka, T. Uemura and S. Tokito, *ACS Appl. Mater. Interfaces*, 2013, **5**, 9670-9677.
48. G. Bussi, D. Donadio and M. Parrinello, *J. Chem. Phys.*, 2007, **126**, 014101.
49. H. J. C. Berendsen, J. P. M. Postma, W. F. van Gunsteren, A. DiNola and J. R. Haak, *J. Chem. Phys.*, 1984, **81**, 3684-3690.
50. M. Parrinello and A. Rahman, *J. Appl. Phys.*, 1981, **52**, 7182-7190.
51. U. Essmann, L. Perera, M. L. Berkowitz, T. Darden, H. Lee and L. G. Pedersen, *J. Chem. Phys.*, 1995, **103**, 8577-8593.
52. S. Kumar, D. Bouzida, R. H. Swendsen, P. A. Kollman and J. M. Rosenberg, *J. Comput. Chem.*, 1992, **13**, 1011-1021.
53. K. Palczynski, G. Heimel, J. Heyda and J. Dzubiella, *Cryst. Growth Des.*, 2014, **14**, 3791-3799.
54. K. J. Thorley, T. W. Finn, K. Jarolimek, J. E. Anthony and C. Risko, *Chem. Mater.*, 2016, **29**, 2502-2512.
55. S. M. Ryno, C. Risko and J. L. Bredas, *J. Am. Chem. Soc.*, 2014, **136**, 6421-6427.
56. J. F. Lutsko, D. Wolf, S. R. Phillpot and S. Yip, *Phys. Rev. B*, 1989, **40**, 2841-2855.
57. Y. L. K. Lu, *Phys. Rev. Lett.*, 1998, **80**, 4474-4477.
58. L. Zhang, Z. H. Jin, L. H. Zhang, M. L. Sui and K. Lu, *Phys. Rev. Lett.*, 2000, **85**, 1484-1847.
59. M. M. Payne, S. R. Parkin, J. E. Anthony, C.-c. Kuo and T. N. Jackson, *J. Am. Chem. Soc*, 2005, **127**, 4986-4987.
60. Y.-L. Loo, *AIChE Journal*, 2007, **53**, 1066-1074.
61. A. K. Hailey, A. J. Petty, J. Washbourne, K. J. Thorley, S. R. Parkin, J. E. Anthony and Y. L. Loo, *Adv. Mater.*, 2017, **29**, 170048.
62. R. Taylor and C. F. Macrae, *Acta Crystallographica Section B*, 2001, **57**, 815-827.
63. I. J. Bruno, J. C. Cole, P. R. Edgington, M. Kessler, C. F. Macrae, P. McCabe, J. Pearson and R. Taylor, *Acta Crystallographica Section B*, 2002, **58**, 389-397.
64. C. F. Macrae, P. R. Edgington, P. McCabe, E. Pidcock, G. P. Shields, R. Taylor, M. Towler and J. van de Streek, *J. Appl. Crystallogr.*, 2006, **39**, 453-457.
65. C. F. Macrae, I. J. Bruno, J. A. Chisholm, P. R. Edgington, P. McCabe, E. Pidcock, L. Rodriguez-Monge, R. Taylor, J. van de Streek and P. A. Wood, *Journal of Applied Crystallography*, 2008, **41**, 466-470.
66. L. Yu, X. Li, E. Pavlica, F. P. V. Koch, G. Portale, I. da Silva, M. A. Loth, J. E. Anthony, P. Smith, G. Bratina, B. K. C. Kjellander, C. W. M. Bastiaansen, D. J. Broer, G. H. Gelinck and N. Stingelin, *Chem. Mater.*, 2013, **25**, 1823-1828.

Table of Contents Graphic